GEOPHYSICS, VOL. 62, NO. 5 (SEPTEMBER-OCTOBER 1997); P. 1533–1543, 9 FIGS.

Imaging complex geologic structure with single-arrival Kirchhoff prestack depth migration

François Audebert*, Dave Nichols‡, Thorbjørn Rekdal**, Biondo Biondi§, David E. Lumley§§, and Hector Urdaneta§

ABSTRACT

We compare various forms of single-arrival Kirchhoff prestack depth migration to a full-waveform, finite-difference migration image, using synthetic seismic data generated from the structurally complex 2-D Marmousi velocity model. First-arrival-traveltime Kirchhoff migration produces severe artifacts and image contamination in regions of the depth model where significant reflection energy propagates as late or multiple arrivals in the total reflection wavefield. Kirchhoff migrations using maximum-energy-arrival traveltime trajectories significantly improve the image in the complex zone of the Marmousi model, but are not as coherent as the finite-difference migration image. By carefully incorporating continuous phase estimates with the associated maximum-energy arrival traveltimes, we obtain single-arrival Kirchhoff images that are similar in quality to the finite-difference migration image. Furthermore, maximum-energy Green's function traveltime and phase values calculated within the seismic frequency band give a Kirchhoff image that is (1) far superior to a first-arrival–based image, (2) much better than the analogous high-frequency paraxial-ray Green's function image, and (3) closely matched in quality to the full-waveform finite-difference migration image.

INTRODUCTION

Kirchhoff prestack depth migration

The Kirchhoff migration method is popular in seismic exploration imaging because of its potential for I/O flexibility and computational efficiency. A major advantage of Kirchhoff migration is the ability to process arbitrary subsets of input or output data. For example, a target-oriented migration can be performed to image a small subset of the complete image, thus saving a great computational expense. Selected input data gathers can be migrated individually to check image quality control. Constant-offset Kirchhoff migrations can be used for tomographic velocity estimation (van Trier, 1990; Etgen, 1990) and AVO analysis (Lumley, 1993). In contrast, non-Kirchhoff methods based on full wavefield extrapolation are constrained to correspond to a physically realizable experiment, which often implies intensive simultaneous processing of large input and output data volumes.

Another major advantage of the Kirchhoff migration method is the ability to accommodate irregular trace spacings. The Kirchhoff migration procedure involves an integration of the seismic wavefield along the recording surface, which in practice is cast as a discrete summation. Irregular sampling of the wavefield along the recording surface is easily handled by the discrete sum. In contrast, Fourier-domain and finite-difference (FD) methods require regular sampling along the recording surface to take advantage of efficient fast Fourier transform (FFT) and FD operator implementations to process the wavefield. Since 3-D seismic data acquisition geometries often produce irregular trace spacings, the Kirchhoff migration method is currently the only practical approach to migrating 3-D prestack seismic data.

Manuscript received by the Editor November 7, 1995; revised manuscript received November 12, 1996.
*Compagnie Generale de Geophysique, 1 Rue Leon Migaux 91341, Massy, France.
‡Formerly Stanford Exploration Project, Dept. of Geophysics, Stanford, California 94305; presently Geco-Prakla, Schlumberger House, Gatwick, RH6 ONZ, United Kingdom. E-mail: nichols@gatewick.geco-prakla.slb.com.
**PGS Seres A. S. Strandveien 4, Box 354, 1324 Lysaker, Norway. E-mail: thorrels@oslo.seres.pgs.com.
§Stanford Exploration Project, Dept. of Geophysics, Stanford, California 94305. E-mail addresses: biondi@sep.stanford.edu; hector@sep.stanford.edu.
§§Formerly Stanford Exploration Project, Dept. of Geophysics, Stanford, California 94305; presently Chevron Petroleum Technology Company, La Habra, California. E-mail: lumley@lahabra.chevron.com.

Kirchhoff Green's functions

A major disadvantage of Kirchhoff migration is that it may fail to image seismic data accurately in the presence of complex seismic velocity structure (Geoltrain and Brac, 1993; Godfrey et al., 1993). This undesirable property is not caused by a breakdown in the theory per se, but by the approximations that are commonly introduced in the representation and calculation of the Green's function traveltime and amplitude functions that define the Kirchhoff migration integral. In the most general case, the exact Green's functions are frequency-dependent, and consequently the Kirchhoff migration is a multidimensional integral of the wavefield with frequency-dependent weights and phase rotations. Unfortunately, the numerical evaluation of such an integral is prohibitively expensive. A practical implementation requires some simplifying assumptions about the form of the Green's functions.

The simplest and least expensive Green's function representation assumes a single wavefield arrival from each source position, given as a single traveltime, amplitude, and phase value at each point in the subsurface. This oversimplification of the Green's function may degrade the quality of the Kirchhoff migration image when a complex velocity field causes multipathing, i.e., when many wavepaths connect a single-source/receiver location with a single depth location.

When multipathing occurs, the use of first-arrival Green's functions computed by finite-differencing the eikonal equation (van Trier and Symes, 1991) or by optimization methods based on Fermat's principle (Moser, 1991) do not yield satisfactory images, as demonstrated in Geoltrain and Brac (1993). This is because first arrivals do not contribute to significant reflection energy below complex velocity overburden. Gray and May (1994) have recently shown that by limiting the propagation angle of a modified finite-difference eikonal solver, and thus selecting arrivals corresponding to a local body-wave traveltime instead of the global first arrival, the Kirchhoff migration image can be improved compared to using first-arrival Green's function traveltimes. Gaussian Beam migration (Hill, 1990) is a promising new variation of the Kirchhoff method that naturally incorporates multipath arrivals in the migration image, but still relies on conventional high-frequency ray assumptions for the Green's function representation.

OUR CONTRIBUTION

In this paper, we demonstrate that a careful choice of a single best arrival that approximates the true multipath arrivals can lead to an accurate Kirchhoff migration image. We show that if the single-valued Green's functions are carefully estimated, the quality of the images produced by Kirchhoff migration in the presence of complex velocity fields is close to the quality of the images produced by full-waveform, finite-difference migration. The key element for achieving this result is the estimation of traveltimes, amplitudes, and phases of the "effective" most-energetic arrival. We also demonstrate the importance of using the correct phase when multiple arrivals are present. Phase rotation of the most energetic arrival is caused by caustics and by phase-mixing when multiple arrivals are superimposed.

We implement two methods for computing the most energetic arrival in a 2-D isotropic velocity model, and compare them with an accurate method for computing the first-arrival traveltime. The first method uses paraxial ray tracing to compute the traveltimes, phases, and amplitudes of seismic arrivals (Keho and Beydoun, 1988; Rekdal and Biondi, 1994). The second method takes into account the band-limited nature of the seismic wavefield by directly solving the Helmholtz equation in the frequency domain for few frequencies within the seismic bandwidth (Nichols, 1996).

In the next section, we review the theoretical foundations of Kirchhoff migration and their relationship with the parameterization of the Green's functions. Next, we discuss three methods for computing Green's functions (first-arrival, paraxial, and band-limited), and discuss their characteristics using a model example. Finally, we show the result of applying these methods of Green's function computation to a Kirchhoff migration of the Marmousi seismic data set.

KIRCHHOFF MIGRATION THEORY

In our implementation of Kirchhoff migration, we define a kinematic prestack depth migration equation that is suitable for either 2-D or 3-D data acquisition and incorporates single-arrival traveltime and phase estimates. In the Appendix, we start with the Helmholtz scalar wave equation (Morse and Feshbach, 1953),

$$\{\nabla^2 + (\omega/v)^2\}P(\mathbf{x}, \omega) = S(\mathbf{x}, \omega), \tag{1}$$

and derive a frequency-domain Kirchhoff prestack depth migration equation (A-8) incorporating the full frequency-dependent Green's functions as

$$R(\mathbf{x}) \approx \int_{\omega}\int_{\mathbf{x}_S}\int_{\mathbf{x}_r} W[\hat{\mathbf{n}} \cdot \nabla G_r(\mathbf{x}, \omega)]G_s^*(\mathbf{x}, \omega) \times P(\mathbf{x}_r, \omega; \mathbf{x}_s)\, d\mathbf{x}_r\, d\mathbf{x}_s\, d\omega. \tag{2}$$

Equation (2) is a weighted zero-lag correlation of the source and reflected wavefields, where W is the migration weight function defined by equation (A-7), G_s and G_r are the source and receiver Green's function solutions to equation (1), P is the recorded scalar seismic data, ω is the temporal angular frequency, and $\mathbf{x}$, $\mathbf{x}_s$, and $\mathbf{x}_r$ are the spatial coordinates of the subsurface, source, and receiver points, respectively. G_s^* is the frequency-domain complex conjugate of G_s. The recording surface $\mathbf{x} = \mathbf{x}_r$ is defined by the unit normal vector $\hat{\mathbf{n}}$.

To proceed, we assume a parametric form for the Green's functions G_a such that:

$$G_a(\mathbf{x}, \omega; \mathbf{x}_a) \approx A_a(\mathbf{x}; \mathbf{x}_a)e^{\pm i(\omega\tau_a + \phi_a)}, \tag{3}$$

where opposite signs are chosen in the exponential for the source (outgoing), and receiver (reverse-time extrapolated) Green's functions, respectively. The parameters A_a, τ_a, and ϕ_a are amplitudes, traveltimes, and phase rotations for a single-arrival Green's function from an arbitrary location $\mathbf{x}_a$ to $\mathbf{x}$. These parameters are often estimated by conventional high-frequency asymptotic ray methods, but may also be estimated within the seismic band as discussed in the Green's function section of this paper.

Given the parametric form (3), an efficient time-domain version of equation (2) can found after an inverse temporal Fourier-transform as follows:

$$R(\mathbf{x}) \approx \int_{\mathbf{x}_S}\int_{\mathbf{x}_r} \cos\theta_r\, \hat{W} e^{i\phi_{sr}}\, \hat{P}(\mathbf{x}_r, \mathbf{x}_s; t = \tau_{sr})\, d\mathbf{x}_r\, d\mathbf{x}_s, \tag{4}$$

where the "obliquity factor" $\cos\theta_r$ is a function of the incident angle at each receiver with respect to the surface normal, and is obtained as the dot product $(v_r \nabla\tau_r \cdot \hat{\mathbf{n}})$. The Kirchhoff space-time migration equation (4) is a weighted diffraction stack of the preprocessed, deconvolved (but not divergence-corrected) data $\hat{P}$, after phase-rotation by the Green's function parameters $\phi_{sr} = \phi_s + \phi_r$, evaluated along the diffraction trajectories given by the Green's function traveltimes $\tau_{sr} = \tau_s + \tau_r$.

The phase rotation is implemented by noting that

$$e^{i\phi_{sr}} = [\cos\phi_{sr} + \sin\phi_{sr}\mathcal{H}], \tag{5}$$

where $\mathcal{H}$ is the Hilbert transform operator which has the frequency-domain representation: $\mathcal{H}(\omega) = i\omega/|\omega|$.

We define *kinematic migration* by setting the migration weights $\hat{W}$ to unity, and explicitly expand the phase rotation operation to derive our desired kinematic Kirchhoff prestack depth migration equation

$$R(\mathbf{x}) \approx \int_{\mathbf{x}_s}\int_{\mathbf{x}_r} \cos\theta_r[\cos\phi_{sr}\,\hat{P}(\mathbf{x}_r, \mathbf{x}_s; t = \tau_{sr}) + \sin\phi_{sr}\,\mathcal{H}\{\hat{P}(\mathbf{x}_r, \mathbf{x}_s; t = \tau_{sr})\}]\, d\mathbf{x}_r\, d\mathbf{x}_s. \tag{6}$$

Equation (6) is suitable for 2-D migration if all spatial coordinates are 2-D vectors, i.e., $\mathbf{x} = (x, z)$, and $\hat{P}$ is preprocessed by the half-time derivative operator $\sqrt{i\omega}$. However, equation (6) is equally suitable for 3-D migration if all spatial coordinates are 3-D vectors, i.e., $\mathbf{x} = (x, y, z)$, and $\hat{P}$ is preprocessed by the full-time derivative ∂_t. Equation (6) gives accurate estimates of reflectivity amplitudes for near-offset data, and provides an efficient and robust structural imaging condition when a full range of offset data is migrated. This can be shown by comparing the amplitude behavior of the dynamic and kinematic imaging conditions defined in Lumley (1989) at near and far offsets.

GREEN'S FUNCTION COMPUTATION METHODS

We compare three different methods for computing parametric Green's functions. The method described in Podvin and Lecomte (1991) represents the first class of methods that computes first-arrival traveltimes in a high-frequency asymptotic limit. Paraxial ray tracing (Beydoun and Keho, 1987) represents the second class of high-frequency methods that can compute multiple and maximum energy arrivals in addition to first arrivals. The third method is a nonhigh-frequency band-limited Green's function computation (Nichols, 1996) that estimates the most energetic arrival for a band-limited wavefield.

Asymptotic Green's functions

Most methods used to compute parametric Green's functions for Kirchhoff migration are based upon the high-frequency ray approximation of the elastodynamic equation. First, *P*- and *S*-waves are assumed to be totally decoupled. Second, a high-frequency approximation is made. In the high-frequency limit the traveltimes are independent of the amplitudes. The raypaths and the traveltimes are found by solving the eikonal equation (Aki and Richards, 1980)

$$\nabla\tau \cdot \nabla\tau - \frac{1}{v^2} = 0. \tag{7}$$

If amplitudes are desired, they can be computed by solving the associated transport equation

$$\nabla^2\tau + 2\frac{\nabla A_0}{A_0} \cdot \nabla\tau = 0. \tag{8}$$

High-frequency methods are only valid if the physical parameters in the medium vary slowly over a wavelength, thus they break down at discontinuity interfaces. This problem can be overcome by using a ray method between interfaces and some other scheme to cross the interface. Snell's law, and phase parameter and ray parameter matching have been used successfully with kinematic and dynamic ray methods in layered media. Unfortunately, the cost of computing all possible arrivals becomes overwhelming when many interfaces are present.

Ben-Menahem and Beydoun (1985) present an analysis of all the ray validity conditions. Most of them are not fulfilled strictly even in quite smooth velocity models. Amplitude and phase appear to be more sensitive than traveltimes to the violation of the ray validity conditions. In practice, traveltimes that are computed in violation of the ray validity conditions are often reasonably accurate estimates of the true traveltimes.

First-arrival traveltimes.—When only first-arrival traveltimes are required, methods based on finite differencing the eikonal, or even simpler methods based on Fermat's principle (Moser, 1991; Podvin and Lecomte, 1991) can be very efficient. We tested Podvin and Lecomte's method, which computes first-arrival traveltimes without amplitude information. Traveltimes are computed at the nodes of a rectangular grid of constant slowness cells. The incremental traveltimes are computed using Huygens' principle, with a local point-source approximation from the nodes and a plane-wave approximation from the edges and faces of the slowness cells. Fermat's principle is invoked to retain only absolute minimum traveltimes. Although more recent implementations allow the tracking of multiple branching and multiple arrivals, we have only tested the method with first-arrival traveltimes. This method always finds the true first-arrival, which may include head-wave arrivals.

Maximum amplitude arrival traveltimes.—As an example of a method that can calculate traveltimes and amplitudes of multiple arrivals, we used a paraxial ray tracing code. The traveltime and curvature of the wavefront are computed from the dynamic ray equations (Beydoun and Keho, 1987). This local approximation to the wavefront is used to estimate the traveltimes in the vicinity of the rays. The dynamic ray-tracing equations are valid in the far-field from a point source and far from singularities in weakly inhomogeneous media. With these provisions, the stationary traveltimes are computed correctly along the central ray. However, the extrapolation of traveltimes in the vicinity of a central ray is very sensitive to errors in the dynamic parameters. Therefore, in rough models a fairly dense fan of rays has to be computed. In practice, some smoothing of the model is usually required to limit the number of rays. As with all ray-based methods, there are "shadow-zones" in the model, which are regions where no geometric ray can be found. The paraxial approximation can be used to estimate traveltimes in these regions, but the estimates become increasingly unreliable at large distances from the ray.

In our tests using paraxial ray tracing, the Green's functions are computed in a smoothed model. The exact model

is smoothed with a Gaussian bell operator, with a half-width equal to the wavelength at a frequency of 30 Hz. If multiple rays give an estimate at the same location, the most energetic arrival is chosen. If two events interfere at the time of the most energetic arrival, they are phase-merged into a single equivalent arrival (Rekdal and Biondi, 1994).

Band-limited Green's functions

The calculation of band-limited Green's functions is a new method that provides a traveltime solution in a user-defined frequency bandwidth rather than in a high-frequency approximation (Nichols, 1996). This approach calculates monofrequency Green's functions for a sparse set of frequencies $G(\omega_j)$ and then finds a parametric model consisting of one or more impulsive events that match these functions. Each impulsive event is characterized by a traveltime τ, amplitude A, and a phase ϕ. We then seek an n-event model that matches the computed frequency-domain Green's function for all frequencies. The Green's function is then simply the sum of the discrete events

$$\sum_{i=1}^{n} A_i e^{i\phi_i} e^{i\omega\tau_i} = G(\omega_j).$$

This implementation is a single-event approximation that seeks to find the traveltime, amplitude, and phase of the maximum energy arrival. A small number of frequencies (8–16) in the seismic frequency band are extrapolated outward from the source location using a paraxial one-wave equation in polar coordinates. At each radius, a parametric approximation to the wavefield is estimated by picking the peak of the Green's function energy within a time window centered around the traveltime at the previous radius. This method is intermediate in cost between calculating all the frequencies of the full Green's function and calculating the solutions at only one frequency, the infinite frequency, as in asymptotic methods.

The main advantage of this method is that the solution is an estimate of the Green's functions in the seismic frequency band, not the Green's function at an unrealistic high frequency, and is therefore more likely to be representative of wave propagation at seismic wavelengths (Biondi, 1992). There are no restrictions on the smoothness of the velocity model with this method.

COMPARISON OF TRAVELTIME TRAJECTORIES

An exploding diffractor test

Since the computed traveltimes play the central role in the Kirchhoff migration integral, they have to be correct or at least correspond to significant events. We compare the traveltimes computed by the three different methods with a full wavefield generated from a point source in the Marmousi velocity model. The model is shown in Figure 1. The source was located at a depth of 2500 m and at a horizontal distance of 6000 m. The wavefield was recorded at the surface. The shot wavefield was modeled with a two-way acoustic finite-difference algorithm, and is displayed as the ideal Green's function in Figures 2–4.

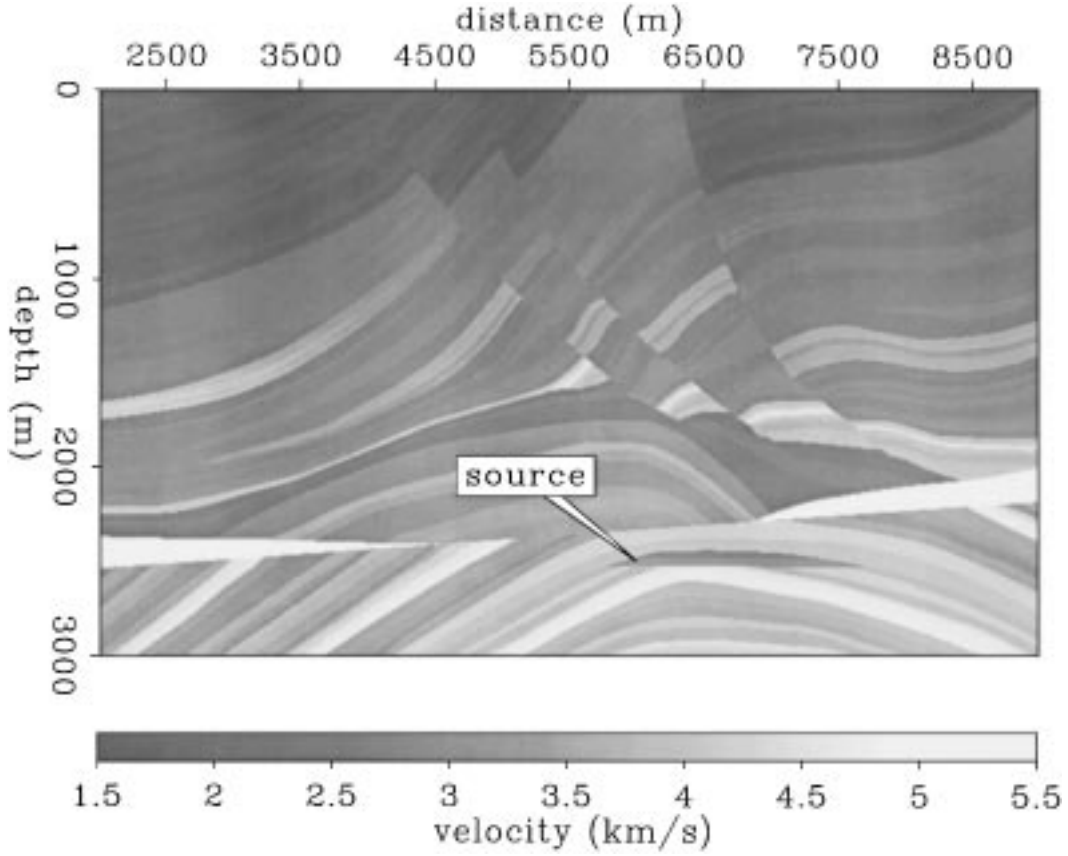

FIG. 1. Marmousi velocity model. The velocity model used to create and migrate the Marmousi seismic data set.

We extracted traveltimes for the various Green's function computation methods from the precomputed tables created for the Kirchhoff migration program. These tables contain traveltimes from regularly sampled surface locations to each point in the subsurface.

The shot experiment as described above is an exploding diffractor experiment. The modeled data represents the true band-limited diffracted wavefield for a exploding diffractor located within the Marmousi reservoir. In a full-waveform migration algorithm, this wavefield would be correlated with the zero-offset field data to obtain an image of the subsurface diffractor location.

Migration diffraction curves

The computed traveltimes define the actual diffraction curve τ_{sr} used in the kinematic Kirchhoff integral of equation (6). The aim of this comparison is to see how much of the true wavefield is captured in the kinematic migration. A perfect migration would integrate the complete wavefield into the point diffractor. Instead the kinematic migration chooses one summation path, defined by one traveltime value for each surface location. All events that lie along this integration path are summed coherently (provided they have a same phase) and properly migrated. Any arrivals not captured by this summation path

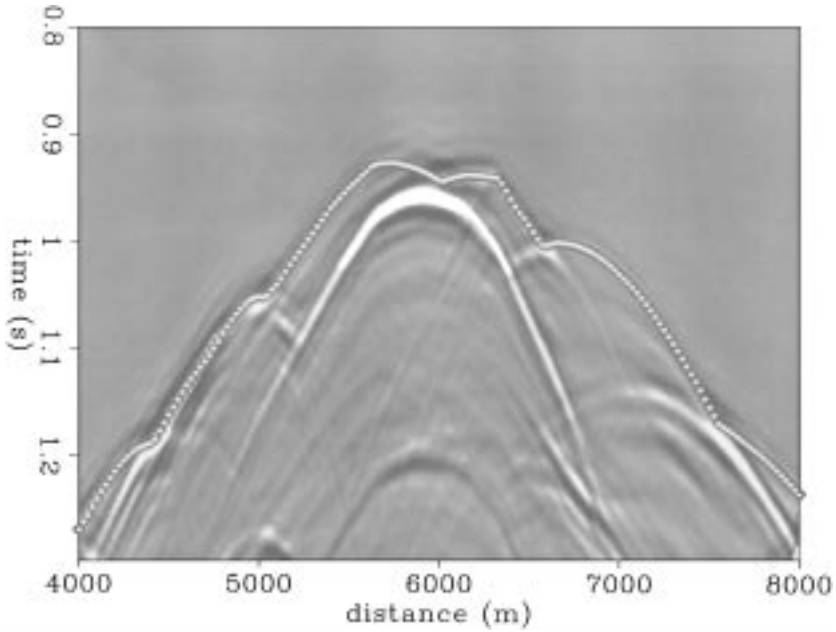

FIG. 2. Podvin's method. First-arrival traveltimes at the surface, for a source at the target depth point.

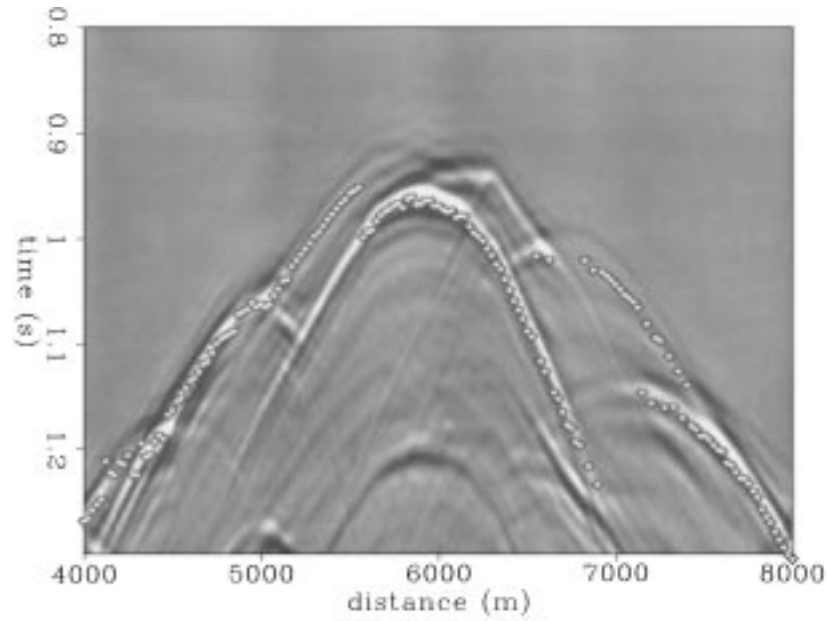

FIG. 3. Paraxial method. Maximum energy arrival traveltimes at the surface, for a source at the target depth point.

are incorrectly over- or undermigrated. The single-event kinematic migration produces the combination of one correctly migrated image from the captured arrivals, together with an overmigrated image from the later arrivals, and an undermigrated image from the earlier arrivals. Unfortunately, those three migrated sections are produced at the same time. They cannot be separated. The hope is that the migrated section produced by the captured arrivals will be more energetic than the other two. This is more likely to be the case if the captured arrivals are the most energetic ones, and if they are summed with a coherent phase rotation.

First-arrival traveltimes.—The first arriving traveltimes calculated by Podvin's method were computed on a resampled version of the original Marmousi velocity model. The original 4×4 m gridded velocity model of Marmousi was resampled to a 12.5×12.5 m grid of constant slowness cells. No smoothing was used except that required by the resampling and only first-arrival traveltimes were computed.

In Figure 2 the computed traveltimes from Podvin's method are superimposed upon the full diffraction wavefield. The traveltimes are plotted as white-filled circles. We observe that this method tracks the first-arrival traveltime accurately. However, the first arrivals contain almost none of the total wavefield energy. Hence, integrating only the first arrivals would not be sufficient to produce a clear image at this depth point. We can expect the remaining energy to be overmigrated and produce artifacts.

Paraxial maximum-amplitude arrivals.—For the asymptotic maximum-amplitude arrivals, we used a grid size of 8×8 m for the velocity model, which was represented with bicubic splines. We used a Runge Kutta solver to solve the dynamic and kinematic ray equations. The density of rays was adapted to give maximum distance between two neighboring rays of 75 m wherever geometrical rays existed.

In Figure 3, the maximum energy arrival computed using the paraxial ray method is overlaid upon the full diffraction wavefield. The method seems to do a good job of picking the most energetic arrivals. A significant portion of the energy is captured. Note however, that some of the arrivals are not zero phase, especially on the central diffraction, which makes judgment of the accuracy of the traveltimes somewhat subjective.

Band-limited traveltimes.—For the purposes of this study, we used 16 frequencies in the 10–60 Hz range in the band-limited traveltime estimation. The velocity model was resampled onto a polar coordinate grid by bilinear interpolation in slowness. The polar grid was sampled every 0.7° in the dip direction and every 11.11 m in the radial direction.

Figure 4 shows the traveltimes computed using this method. As with the paraxial ray tracing, the arrivals may not be zero phase, so the traveltimes overlaid on the modeled data may be half a wavelength away from a peak. On the whole this method does a good job of picking out the maximum energy arrival at each location. In a few places, it chooses an event that is weaker apparently than another. This may be caused by either an inaccuracy of the method for selecting the maximum-energy arrival, or by our use of a one-way wave equation in the traveltime calculation and a two-way wave equation in the FD modeling code.

COMPARISON OF MIGRATION IMAGES

In this section, we compare a variety of Kirchhoff prestack depth migrations to a reference full-waveform finite-difference migration of the 2-D Marmousi seismic data set. The Marmousi prestack data consist of 240 synthetic marine shot gathers modeled over the complex velocity model shown in Figure 1. Each shot gather contains 96 traces at a record length of 2.9 s sampled at 4 ms intervals. The seismic data were generated by acoustic two-way, finite-difference wave-equation modeling (Versteeg and Grau, 1990).

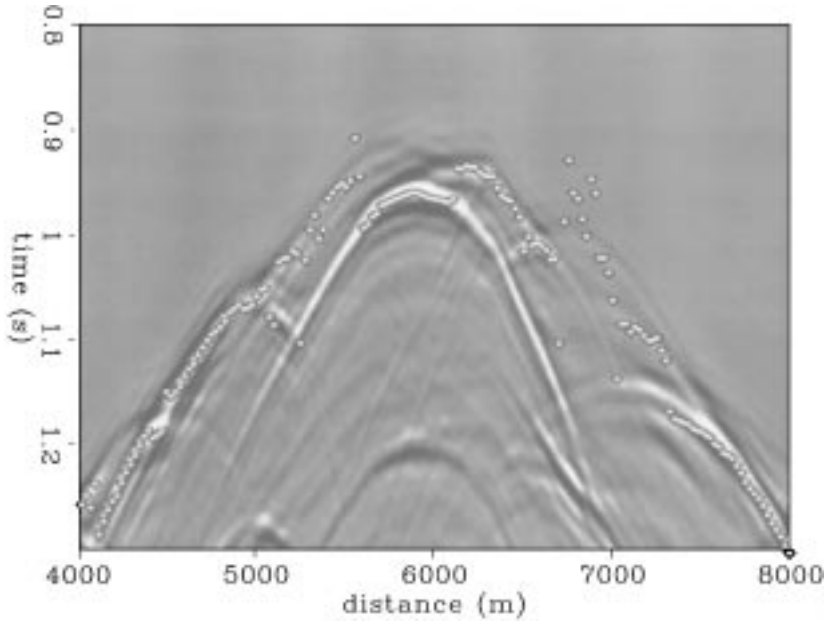

FIG. 4. Band-limited method. Maximum energy arrival traveltimes at the surface, for a source at the target depth point.

We have used the exact Marmousi velocity model for both the finite-difference and Kirchhoff migrations. Some of the Green's function methods internally smooth the input velocity model to satisfy ray validity conditions, ensure numerical stability, and approximate frequency-dependent behavior, as discussed in the previous section. In reality, a model of this complexity cannot be realistically estimated from field seismic data. Our choice of the exact Marmousi model demonstrates that Kirchhoff migrations can image at least as well as finite difference shot profile migration if they are both provided with the velocity model that generated the seismic reflection data.

Finite-difference, shot-profile migration

To assess the quality of our Kirchhoff migrations, we chose a finite-difference shot profile migration of the Marmousi data as our ideal reference image. We used a one-way, 70°, explicit finite-difference wave propagation algorithm, with the standard cross-correlation imaging condition. As is common practice, we divergence-corrected the shot gather data prior to shot profile migration to balance the output image amplitudes. In contrast, the data are not divergence-corrected prior to Kirchhoff migration because Kirchhoff migration weights can perform the (potentially more accurate) amplitude recovery internally during the migration procedure.

The shot-profile–migrated image inherently incorporates the multi-arrival and band-limited nature of seismic data by directly solving the wave equation with a finite difference operator. Figure 5 shows the finite-difference, shot-profile migration to be an excellent image of the Marmousi model and serves as a reference image to calibrate our Kirchhoff migration images. We will show in the following sections that, with careful Green's function evaluation criteria, we can obtain a single-arrival Kirchhoff migration image that matches the quality of this reference migration image.

Kirchhoff prestack depth migrations

In the next three subsections, we compare several modes of Kirchhoff prestack depth migration to the reference finite-difference shot-profile image. All of our Kirchhoff migration images employ the kinematic imaging condition defined by equation (6). Each migration uses the same Kirchhoff code and differs only in the method of creating the Green's function tables, which are precomputed and accessed on-the-fly in the migration algorithm.

Since we can expect substantial differences in the amplitudes obtained by Kirchhoff migration and finite-difference, shot profile migration, we chose to limit our comparison only to kinematic Kirchhoff migration images. More accurate dynamic Kirchhoff migrations could be obtained by explicit use of the Green's function amplitude values in the Kirchhoff migration weight factor (Bleistein, 1987; Lumley, 1989; Schleicher et al., 1993; Lumley, 1993).

First-arrival traveltime migration

Our first example of Kirchhoff migration uses only first-arrival traveltime information as computed by the method of Podvin and LeComte (1991) and assumes that the phase delay term ϕ_{sr} is zero everywhere. The Kirchhoff migration image created using first-arrival traveltimes is displayed in Figure 6.

The image is inferior to the reference shot-profile image. A similar result was discussed in Geoltrain and Brac (1993). The major problem is that in deep sections of the model, the first-arrival traveltimes correspond to reflection and refraction events with little or no energy, as we demonstrated by the Green's function overlay of Figure 2. Furthermore, the first-arrival traveltimes are earlier (by definition) than the later more-energetic arrivals, and therefore give rise to strong over-migration artifacts in the deep parts of the image. In the shallow parts of the image where multiple arrival path are not an issue the first-arrival migration seems adequate. However, the

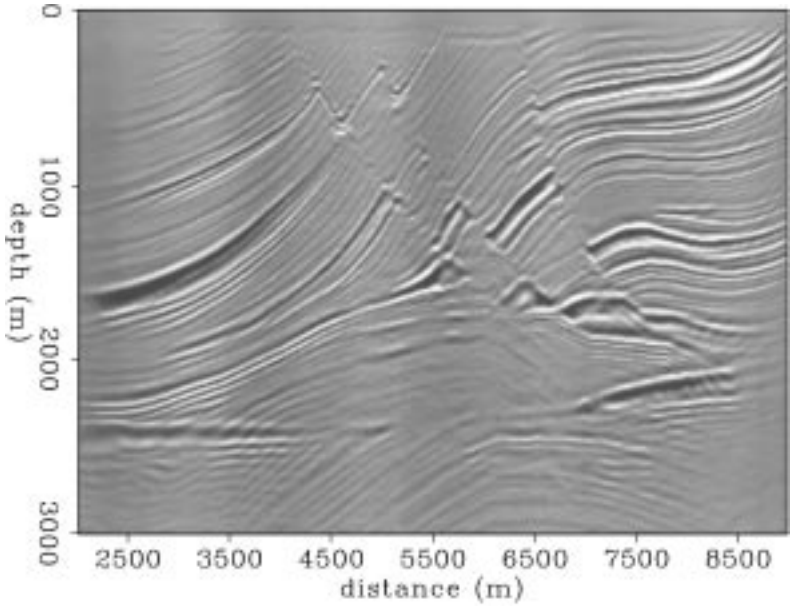

FIG. 5. The full-waveform migrated image obtained with a finite-difference shot-profile migration and a correlation imaging condition.

artifacts caused by nonenergetic summation trajectories along late energetic reflection events cause serious contamination of the image in the vicinity of the reservoir target zone. Hence, we interpret these results to signify that first-arrival traveltime migration is useful only when the first arrival is the most energetic. This corresponds to the situation in which velocity models exhibit weak lateral velocity variation.

Maximum-energy traveltime migration

The Green's function overlays of Figures 2, 3, and 4 suggest that an improved single-arrival Kirchhoff migration can be obtained by computing the traveltime field associated with the most energetic arrival. Summation along maximum energy trajectories should capture more significant energy in the reflected wavefield than the first-arrival method.

Figure 7 compares Kirchhoff migrations generated from maximum-energy traveltimes calculated by the paraxial and band-limited methods with the images generated using first-arriving traveltimes. As in the previous image, the phase shift is assumed to be zero. Both maximum-energy traveltime images are superior to the first-arrival image, especially in the central complex portion of the model, where the first-arrival overmigration artifacts have been suppressed. The band-limited image is slightly more coherent than the paraxial image, especially in the reservoir, and in the overlaying dipping reflectors and fault truncations. However, these images are still not as accurate as the finite-difference migration. The maximum-energy traveltime images are not as crisp or coherent as the shot profile reference image, and there are undesirable fluctuations in amplitude and waveform character along some reflectors, indicating that some reflection energy has not yet been optimally stacked. In the next section, we show that incorporating phase information into the maximum-energy traveltime migration improves these images considerably.

MAXIMUM-ENERGY TRAVELTIME/PHASE MIGRATION

Maximum-energy arrivals may require some phase rotation associated with a traveltime to coherently sum along the same phase of a waveform. Such phase rotations arise naturally from two causes: first, the existence of caustics, which give rise to phase shifts in integer multiples of $\pi/2$; and second, superposition of multiple arrivals that yield an effective most energetic arrival that may have an arbitrary phase rotation. The two maximum-energy methods discussed in this paper are capable of estimating the phase rotation associated with both phenomena. Consequently, we incorporate the phase rotations in the imaging traveltimes to ensure that coherent energy is summed along a consistent phase of the waveform.

Figure 8 shows a comparison of Kirchhoff migration images using traveltime estimates only, and those created using traveltime and phase estimates together. The images created using the additional phase information are more coherent than their traveltime-only counterparts. The improvement demonstrates that phase rotations are significant in the complex central portion of the model. In particular, the reservoir reflection and overlaying dipping reflectors and fault truncations are imaged more clearly. The band-limited image is clearly superior to the paraxial image in these same regions, possibly indicating that a band-limited estimation of the effective arrival phase in the seismic frequency range is a better approximation of the full wavefield than a high-frequency ray estimation of caustic and merged phase.

Finally, Figure 9 compares the two maximum-energy traveltime and phase images with the full-wavefield finite-difference migration image. It illustrates that the single-arrival Kirchhoff prestack depth migration using maximum-energy arrival times and phase rotations is as accurate as the full wavefield finite-difference shot profile migration. The band-limited Kirchhoff image is more coherent than the paraxial image along the deep reservoir reflections and the overlaying dipping reflections. We believe this comparison to be one of the first published

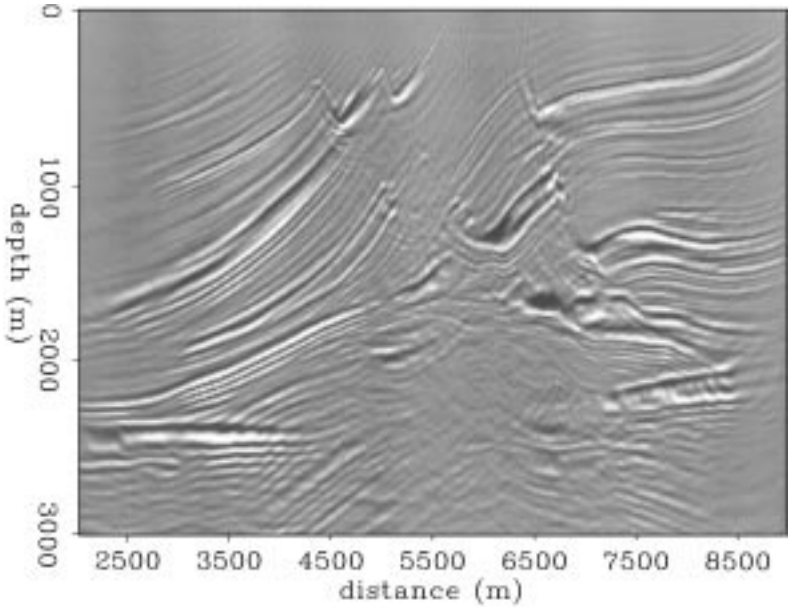

FIG. 6. The Kirchhoff-migrated image obtained using first-arrival traveltimes.

examples of a single-arrival Kirchhoff migration attaining comparable quality to that of a finite-difference migration in an extremely complex velocity structure.

CONCLUSION

We have compared a variety of single-arrival Kirchhoff prestack depth migration images to a reference finite-difference shot-profile migration image, using seismic data generated from the highly complex Marmousi velocity model. We found that first-arrival traveltime Kirchhoff migration produced severe artifacts when reflectors were illuminated by multiple wavepaths.

We demonstrated that Kirchhoff migrations using maximum-energy traveltimes significantly improved the image in the complex zone of the Marmousi model, when compared to the first-arrival traveltime image. Nevertheless, those images were still not as coherent as the finite-difference migration image. However, by adding a phase-rotation term to the imaging algorithm, we obtained single-arrival Kirchhoff images that are comparable in quality to the finite-difference migration image. Furthermore, we demonstrated that using nonasymptotic Green's function values calculated within the seismic bandwidth produced an image that was superior to the image obtained using high-frequency paraxial ray Green's functions.

Finally, we believe our band-limited Kirchhoff migration image may be one of the first published examples of a Kirchhoff migration attaining comparable quality to a finite-difference migration in extremely complex velocity structure. This result is encouraging since, at present, there are no practical prestack imaging alternatives for 3-D seismic data sets other than the Kirchhoff migration method.

ACKNOWLEDGMENTS

During this study, T. Rekdal was funded by the Norwegian Science Foundation (NFR) under the PROPETRO program and Norsk Hydro A/S. F. Audebert was a visitor at the Stanford Exploration Project, supported by Compagnie Generale de Geophysique. All authors were partially or completely supported by the sponsors of the Stanford Exploration Project at Stanford University. The shot-profile finite-difference migration was performed using ProMAX software from Advance Geophysical.

REFERENCES

Aki, K., and Richards, P. G., 1980, Quantitative seismology: Theory and methods: W. H. Freeman and Co.

Ben-Menahem, A., and Beydoun, W. B., 1985, Range of validity of seismic ray beam methods in general inhomogenous media—I. General theory: Geophys. J. Roy. Astr. Soc., **82**, 207–234.

Beydoun, W. B., and Keho, T. H., 1987, The paraxial ray method: Geophysics, **52**, 1639–1653.

Biondi, B., 1992, Solving the frequency-dependent eikonal equation: 62nd Ann. Internat. Mtg., Soc. Expl. Geophys., Expanded Abstracts, 1315–1319.

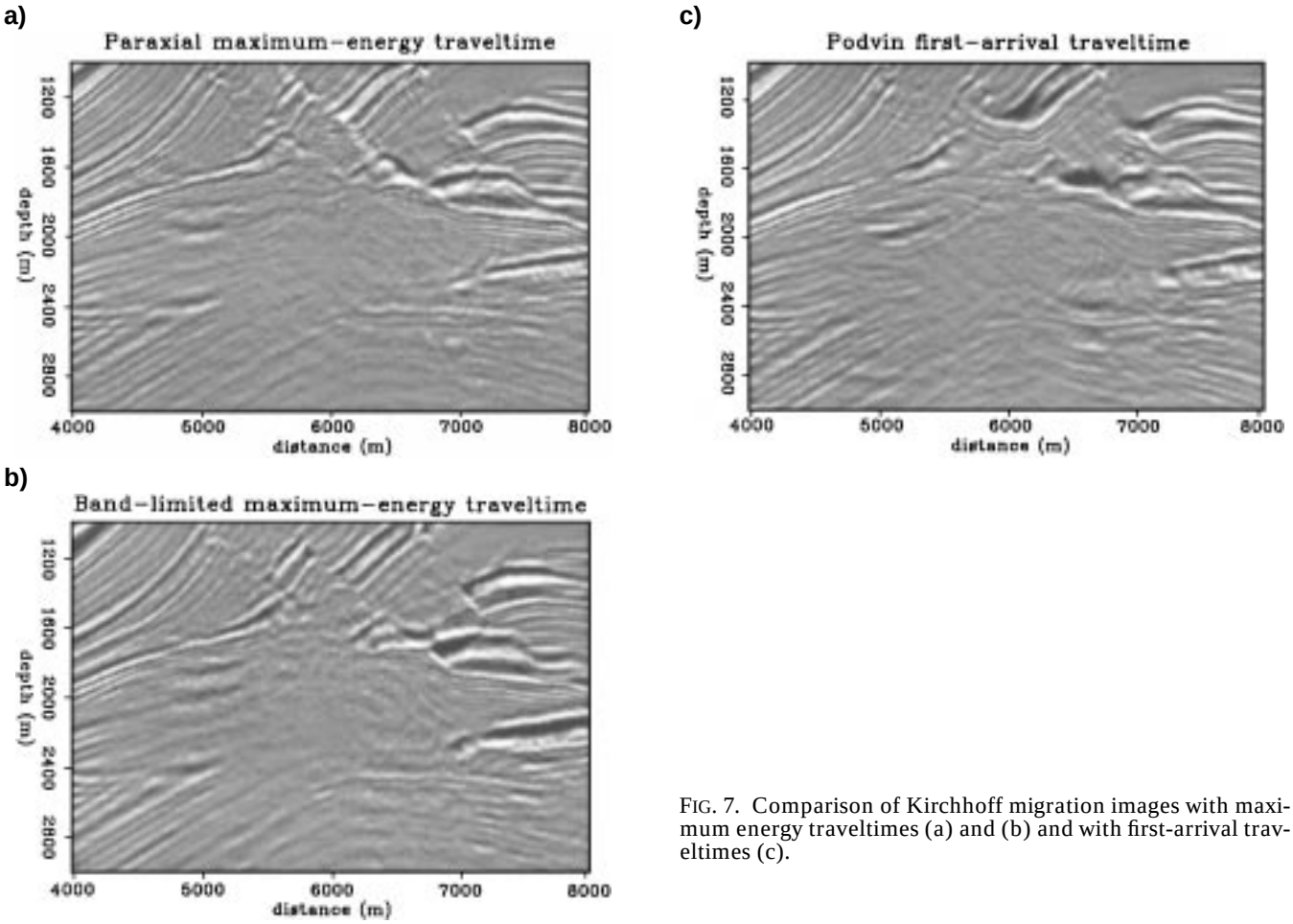

FIG. 7. Comparison of Kirchhoff migration images with maximum energy traveltimes (a) and (b) and with first-arrival traveltimes (c).

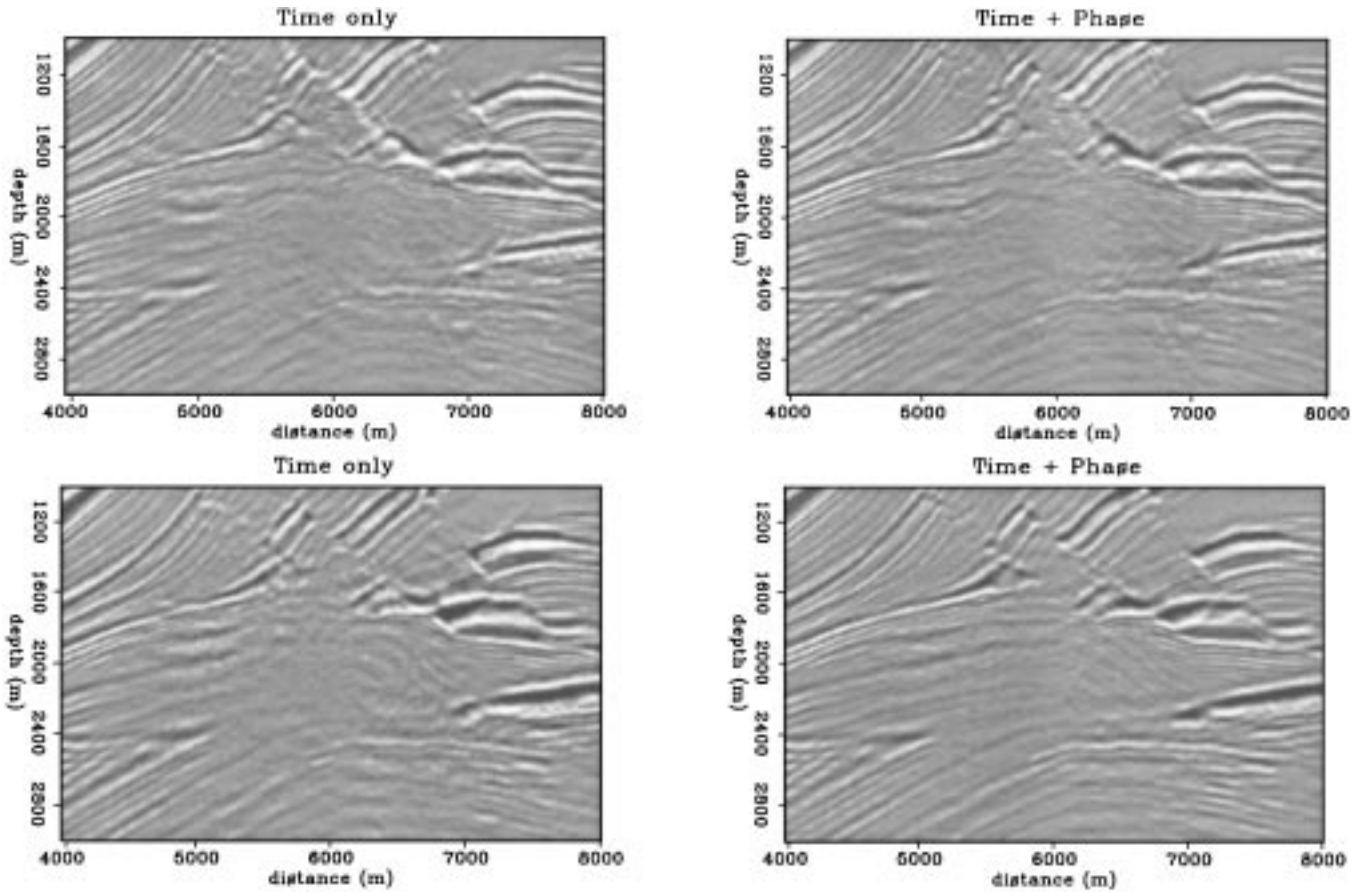

FIG. 8. Comparison of Kirchhoff migration images with traveltimes only versus using both traveltime and phase. The top row uses paraxial ray Green's functions, the bottom row uses band-limited Green's functions.

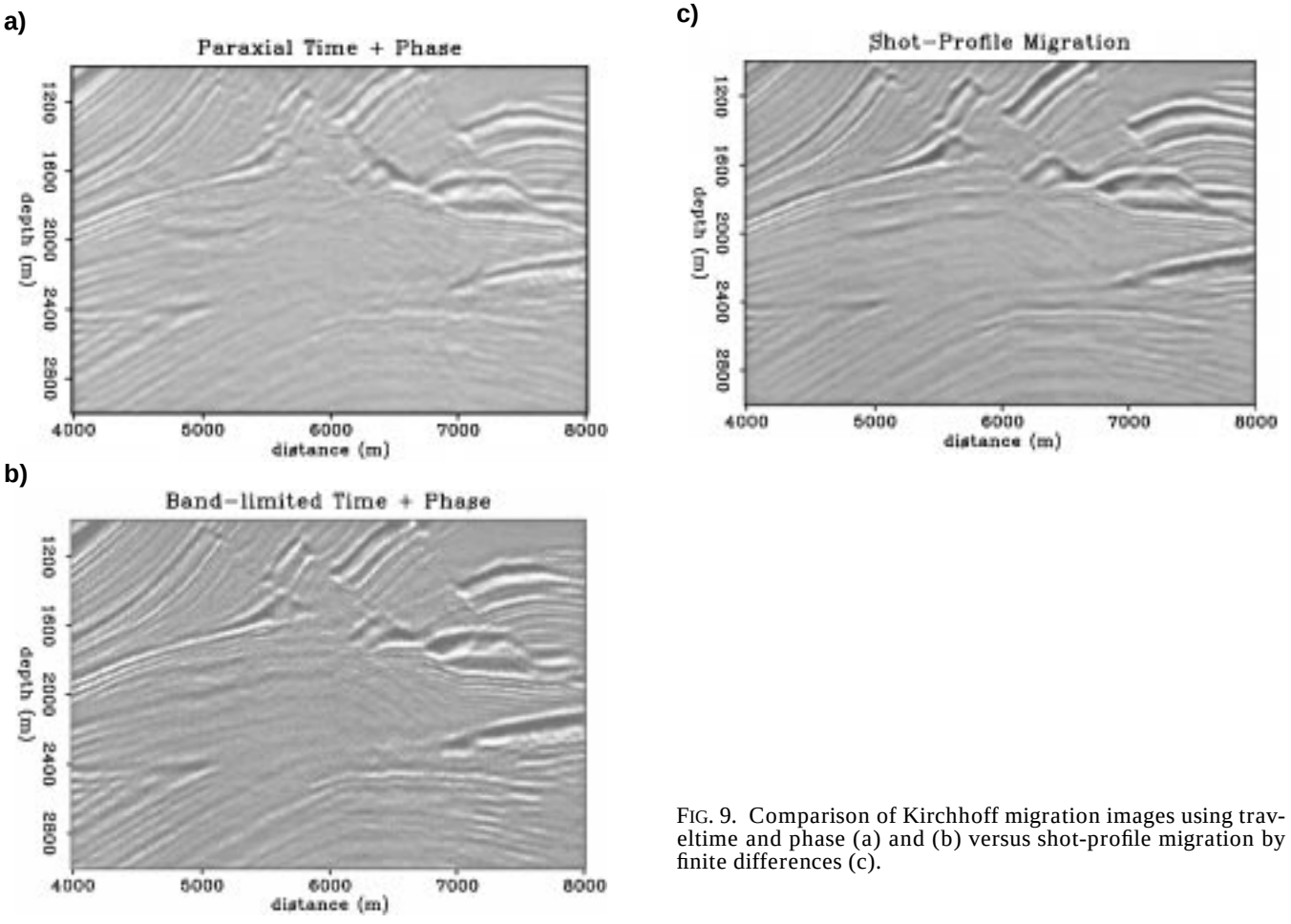

FIG. 9. Comparison of Kirchhoff migration images using traveltime and phase (a) and (b) versus shot-profile migration by finite differences (c).

Bleistein, N., 1987, On the imaging of reflectors in the earth: Geophysics, **52**, 931–942.
Claerbout, J. F., 1971, Toward a unified theory of reflector mapping: Geophysics, **36**, 467–481.
Etgen, J., 1990, Residual prestack migration and interval velocity estimation: SEP-**68**.
Geoltrain, S., and Brac, J., April 1993, Can we image complex structures with first-arrival traveltime?: Geophysics, **58**, 564–575.
Godfrey, B., Pieprzak, A., Berg, K., and Yilmaz, O., 1993, 3-D salt and sub-salt imaging strategy: A case history from the Gulf of Mexico: Presented at Summer Research Workshop, 3-D seismology: Integrated comprehension of large data volumes, Soc. Expl.Geophys.
Gray, S. H., and May, W. P., May 1994, Kirchhoff migration using eikonal equation traveltimes: Geophysics, **59**, 810–817.
Hill, N. R., 1990, Gaussian beam migration: Geophysics, **55**, 1416–1428.
Keho, T. H., and Beydoun, W. B., 1988, Paraxial ray Kirchhoff migration: Geophysics, **53**, 1540–1546.
Lumley, D. E., 1989, Kirchhoff prestack depth migration: Imaging conditions and amplitude recovery: 59th Ann. Internat. Mtg., Soc. Expl. Geophys., Expanded Abstracts, 1336–1339.
———1993, Angle-dependent reflectivity estimation: 63rd Ann. Internat. Meeting, Soc. Expl. Geophys., Expanded Abstracts, 746–747.
Morse, P. M., and Feshbach, H., 1953, Methods of theoretical physics: McGraw-Hill Book Co.
Moser, T. J., 1991, Shortest path calculation of seismic rays: Geophysics, **56**, 59–67.
Nichols, D. E., 1996, Maximum energy traveltimes calculated in the seismic frequency band: Geophysics, **61**, 253–263.
Podvin, P., and Lecomte, I., 1991, Finite-difference computation of traveltimes in very contrasted velocity models: A massively parallel approach and its associated tools: Geophys. J. Internat., **105**, 271–284.
Rekdal, T., and Biondi, B., 1994, Paraxial ray tracing in the Marmousi model: 64th Ann. Internat. Meeting, Soc. Expl. Geophys., Expanded Abstracts, 1406–1409.
Schleicher, J., Tygel, M., and Hubral, P., 1993, 3-D true-amplitude finite-offset migration: Geophysics, **58**, 1112–1126.
van Trier, J., 1990, Tomographic determination of structural velocities from depth migrated seismic data: SEP-**66**.
van Trier, J., and Symes, W. W., 1991, Upwind finite-difference calculation of traveltimes: Geophysics, **56**, 812–821.
Versteeg, R., and Grau, G., 1990, Practical aspects of seismic data inversion, the Marmousi experience, Eur. Assoc. Expl. Geophys., Proc. 1990 EAEG Workshop, 52nd EAEG Meeting, 1–194.

APPENDIX A

KIRCHHOFF MIGRATION THEORY

We briefly derive a frequency-domain Kirchhoff prestack depth migration equation that is suitable for either 2-D or 3-D data acquisition and incorporates the full frequency-dependent Green's function solution to the Helmholtz scalar wave equation.

Source wavefield

Given the Helmholtz variable-velocity v scalar wave equation (Morse and Feshbach, 1953),

$$\{\nabla^2 + (\omega/v)^2\}P(\mathbf{x}, \omega) = S(\mathbf{x}, \omega), \qquad \text{(A-1)}$$

the "downgoing wavefield" D generated by a single source at location $\mathbf{x}_s$ can be evaluated at any subsurface location $\mathbf{x}$ within a volume $\mathcal{V}$ from the frequency-domain integral representation

$$D(\mathbf{x}, \omega; \mathbf{x}_s) = \int_{\mathcal{V}} G(\mathbf{x}, \omega; \mathbf{x}')S(\mathbf{x}', \omega; \mathbf{x}_s)\, d\mathbf{x}', \qquad \text{(A-2)}$$

where $G(\mathbf{x}, \omega; \mathbf{x}')$ is the Green's function solution to equation (A-1) associated with a generic source location $\mathbf{x}'$, and S is the source wave function. If we neglect the absolute amplitude of the source and consider only relative amplitudes in the migrated section, and also assume the source has a compact delta function shape in both space and time, $\delta(t)\delta(\mathbf{x}' - \mathbf{x}_s)$, then the downgoing wavefield can be approximated after the volume integration by the source Green's function G_s alone as

$$D(\mathbf{x}, \omega; \mathbf{x}_s) \approx G(\mathbf{x}, \omega; \mathbf{x}_s) = G_s(\mathbf{x}, \omega). \qquad \text{(A-3)}$$

Reflected wavefield

The "upgoing wavefield" U reflected from the subsurface $\mathbf{x}$ caused by a source at $\mathbf{x}_s$ can be reconstructed from the seismic scalar data P recorded at receivers $\mathbf{x}_r$ using a Kirchhoff boundary integral representation,

$$U(\mathbf{x}, \omega; \mathbf{x}_s) = \int_{\mathcal{S}} \hat{\mathbf{n}} \cdot \nabla G_r(\mathbf{x}, \omega)P(\mathbf{x}_r, \omega; \mathbf{x}_s)\, d\mathbf{x}_r, \qquad \text{(A-4)}$$

where $G_r = G(\mathbf{x}, \omega; \mathbf{x}_r)$ is the receiver Green's function, and $\hat{\mathbf{n}}$ is the unit vector normal to the recording surface $\mathcal{S}$ that bounds the image volume $\mathcal{V}$ of interest. The gradient operator ∇ is taken with respect to the subsurface coordinate $\mathbf{x}$ along the recording surface at $\mathbf{x} = \mathbf{x}_r$.

Reflectivity imaging condition

Given that the reflected wavefield $U(\mathbf{x}, \omega)$ in the vicinity of $\mathbf{x}$ can be modeled as a local time-domain convolution of the subsurface reflectivity $R(\mathbf{x})$ with the source wavefield $D(\mathbf{x}, \omega)$,

$$U(\mathbf{x}, \omega) \approx R(\mathbf{x})D(\mathbf{x}, \omega), \qquad \text{(A-5)}$$

a local least-squares estimate of the frequency-independent reflectivity $R(\mathbf{x})$ can be obtained as the weighted zero-lag correlation of the source and reflected wavefields (Claerbout, 1971)

$$R(\mathbf{x}) \approx \sum_{\omega} WUD^* \approx \sum_{\omega} \frac{U(\mathbf{x}, \omega)D^*(\mathbf{x}, \omega)}{D(\mathbf{x}, \omega)D^*(\mathbf{x}, \omega)}, \qquad \text{(A-6)}$$

where D^* is the complex conjugate of D, and the correlation UD^* is normalized by the local energy of the source wavefield DD^*. Substituting the source wavefield approximation (A-3), the migration weight W reduces to

$$W^{-1} = DD^* \approx G_s(\mathbf{x}; \omega)G_s^*(\mathbf{x}, \omega) = |G_s|^2, \qquad \text{(A-7)}$$

as previously shown in Lumley (1989).

Migration equation

If the weighted zero-lag correlation of equation (A-6) is averaged over all single shot-profile migrations to provide a complete image of the subsurface, the frequency-domain Kirchhoff migration equation becomes

$$R(\mathbf{x}) \approx \int_{\omega}\int_{\mathbf{x}_S}\int_{\mathbf{x}_r} W[\hat{\mathbf{n}} \cdot \nabla G_r(\mathbf{x}, \omega)]G_s^*(\mathbf{x}, \omega) \times P(\mathbf{x}_r, \omega; \mathbf{x}_s)\, d\mathbf{x}_r\, d\mathbf{x}_s\, d\omega, \qquad \text{(A-8)}$$

where the migration weight W is given by equation (A-7). Different migration weights can be derived for alternate processing geometries such as common-receiver or common-offset migrations (Bleistein, 1987; Schleicher et al., 1993; Lumley, 1993).